Flow of bidisperse suspensions under the effect of standing bulk acoustic waves

A. Nath [1] and A. K. Sen [1,2,*]

[1] *Fluid Systems Laboratory, Department of Mechanical Engineering, Indian Institute of Technology Madras, Chennai-600036, Tamil Nadu, India*

[2] *Micro Nano Bio-Fluidics Group, Indian Institute of Technology Madras, Chennai-600036, Tamil Nadu, India*

(Received 18 February 2022; accepted 23 September 2022; published 13 October 2022)

Acoustic handling of dense suspension of microparticles has relevance in lab-on-a-chip, food, and pharmaceutical technologies. So far the studies on acoustic focusing of dense suspensions treat the particles to be of the same size, i.e., monodisperse. Here, the flow of dense bidisperse suspensions of microparticles in a microfluidic channel flow exposed to a standing acoustic wave field is studied. Experiments show selective enrichment of the larger particles along the channel center where the smaller particles are depleted. A continuum-based model reveals that the particle migration is governed by the combined influence of shear-induced migration and acoustic radiation forces. The migration behavior of the suspended particles along the channel length is quantified in terms of the degree of focusing, relating to the particle migration toward the center of the channel, and the degree of segregation, relating to the separation of larger and smaller particles. It is observed that both the degree of focusing and segregation varies directly with the intensity of the acoustic field and the ratio of particle sizes and inversely with the suspension volume fraction.

DOI: 10.1103/PhysRevFluids.7.104201

I. INTRODUCTION

Many naturally occurring and chemically synthesized particles are obtained as "*dense*" suspensions, consisting of a large concentration of particles (typically volume fraction >0.1) in a suspending fluid. The most well-known among these is blood, which is a dense polydisperse suspension consisting of different types of cells. Concentration and manipulation of particles in suspensions is of considerable interest in microfluidics as it has significant applications in several biochemical assays and helps in advancing lab-on-a-chip technologies [1]. Similarly, microfluidic devices are also increasingly finding relevance in manipulation of dense suspensions in food and pharmaceutical industries [2,3]. Segregation of particles of different sizes in bidisperse and polydisperse suspensions under shear flows have been previously reported [4–6]. Due to higher shear-induced migration, relatively larger-sized particles travel across the streamlines faster leading to segregation from smaller-sized particles.

Depending on the scale of flow of the suspension, the modeling of a simple suspension flow needs to take into account various effects [7,8]. For example, when the range of particle sizes in the suspension is of the order of 1–10 μm, shear-induced migration is the dominant mechanism controlling particle migration in a sheared flow [9]. For smaller submicron-sized particles, Brownian diffusion plays an increasingly important role in determining particle motion [10]. While passive forces in dense suspension flows enable applications including sorting, segregation and in microfiltration [11], active forces from externally induced fields enable applications requiring higher

*ashis@iitm.ac.in

throughput and shorter channel lengths. In particular, the flow of suspensions under the influence of an externally induced acoustic field is of interest, due to the noncontact, biocompatible nature of acoustic forces. Although a wide range of applications such as particle and cell sorting, separation [12,13], trapping [14,15], and characterization [16] in microchannel flows using acoustic fields have been studied both experimentally and numerically in literature, they mostly involve suspensions with low concentration of cells or particles (of volume fraction <0.1), i.e., dilute suspensions. A few previous works have looked at working with larger particle concentrations with an aim of reducing the dilution of biological samples [17–20] or concentration of bioparticles into small clusters [21–23]. Further, acoustofluidic techniques are being explored in newer areas of application, for example, in the separation of microplastics from industrial effluents [24]. In this direction, the effect of different phenomena associated with concentrated suspensions finds renewed interest in the field of acoustofluidics.

The existing studies in literature on acoustofluidic flows of dense suspensions treat the suspensions to be comprising particles of the same size, i.e., monodisperse suspensions. For the case of suspensions containing particles of different sizes at high concentrations, the impact of acoustic field forces combined with shear-induced effects on particle migration has not been explored either through experiments or theoretical models. In this study, an investigation into the flow of dense bidisperse suspensions in microchannels under the influence of an acoustic standing wave field is performed experimentally and numerically. Experiments are conducted in a straight microchannel where the flowing suspension containing polystyrene microspheres is exposed to an acoustic standing wave. The standing wave is formed in the half-wave mode along the width of the channel, perpendicular to the direction of flow, with pressure node along the channel center and pressure antinodes at the walls. To explain the different experimental observations, we study numerically the relative influence of different effects on particle motion. In the numerical formulation, we use a continua-based diffusive flux model (DFM) which is originally developed based on studies on flow of monodisperse suspensions [8,25,26] and later expanded to polydisperse suspensions containing particle species of different sizes [27]. Specifically, for the case of bidisperse suspensions, we compare the predictions of the theoretical model with experimental results. First, results from the numerical model for shear flow of freely suspended particles in the absence of external fields is validated with reported results from literature [28]. Later, the acoustic force formulation is introduced and results from the model are observed to correspond well with the present experiments. The concentration profiles obtained from the model are quantified in terms of nondimensional parameters: the Strouhal number (St) relating to the relative timescale of migration to advection, the particle size ratio and the particle volume fractions. The numerical framework and the results obtained in the present work could provide guidelines for efficient design of acoustofluidic devices for separation of particles in high-concentration suspensions.

II. EXPERIMENTAL

A. Device fabrication and experimental setup

The microfluidic channel is fabricated on a $4''$ $\langle 100 \rangle$ the silicon wafer of 200 μm thickness. The wafer is patterned with a positive photoresist (MICROPOSIT S1813) by standard photolithography techniques. The channels are etched through the entire thickness of the wafer (through-etched) using the DRIE etching technique. The main channel has cross-sectional dimensions of 400 μm (W, width) $\times$ 300 μm (H, height) and a total length L = 2 cm [see Figs. 1(a) and 1(b)]. To seal the channels, 500-μm-thick borosilicate glass lids are anodically bonded to both the top and bottom by applying a 1000 V bias at a temperature of 450°C. A piezoceramic PZT transducer (American Piezo) with rated resonant frequency 2 MHz is attached to the bottom glass lid using an epoxy adhesive. To enable fluidic access, inlet and outlet holes are drilled into the glass lid on top using CNC micro-milling and connected to PTFE tubing. The fluids are introduced into the channel by connecting the inlet ports to high-performance syringe pumps (i890neMESYS pump, Cetoni, Germany). To visualize the flow

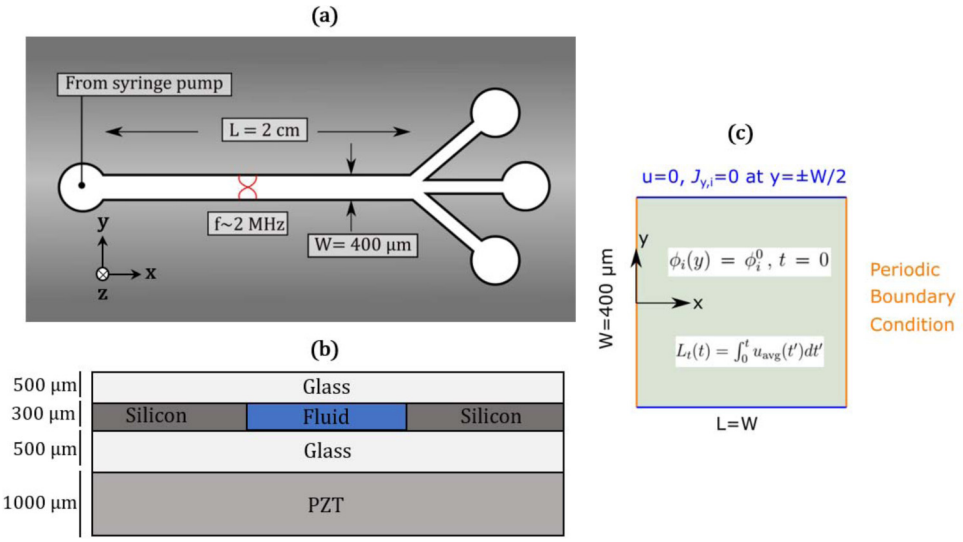

FIG. 1. (a) Schematic of the acoustofluidic device (not to scale) showing a single (central) inlet is used to introduce the suspension into the main channel which branches into a trifurcated outlet. (b) Cross-sectional view showing the different layers. (c) The governing equations are solved in a square computational domain with W = L = 400 μm with appropriate boundary conditions as shown.

of the suspension and image particle concentration profiles, laser scanning confocal microscopy (FV3000RS, Olympus) is used. The flowing suspension is illuminated with two lasers: one with peak wavelength 488 nm and excitation bandwidth ± 20 nm, and the other with peak wavelength 561 nm and excitation bandwidth ± 20 nm. The lasers are used sequentially and therefore images of fluorescent channels are collected separately (sequential imaging instead of simultaneous imaging) to reduce fluorescence bleed through/cross talk effects [29,30]. The bandpass filters direct emitted light of two distinct ranges of wavelengths at 510–540 nm and 600–660 nm into separate detector channels. Here, the detector channel bandwidth is chosen to minimize bleed through artifacts (see Supplemental Material Fig. S1 [31]). An objective lens with 20× magnification and numerical aperture 0.45 is used. At stable particle configuration under acoustic actuation, we first manually focus on the top and bottom channel walls using brightfield images. The top and bottom walls represent the two end z sections between which imaging is performed. Images at different z locations are then obtained by scanning between the two end z sections through step-by-step increments in the focus, and the averaging of images in the z stack is performed using ImageJ.

B. Acoustic actuation

The piezoceramic transducer (PZT) is actuated with a sinusoidal signal generated using a function generator (SMC100A, Rohde & Schwarz) and amplified with an amplifier (75A100A, Amplifier Research) operating in the power range 1–10 W. The resonant frequency of the device is found out by tracking polystyrene beads (of size 10 μm) which are continuously introduced into the main channel as the frequency of actuation is varied over the range 1.9–2.1 MHz in steps of 10 kHz. The particle alignment along the pressure nodal plane was seen to occur fastest at a resonant frequency of 2.02 MHz. The acoustic energy density (E_{ac}) of the system is computed at different operating voltages using a previously reported technique [32]. A dilute suspension of polystyrene particles is introduced to the system, and under stop flow conditions the particle time-location data is tracked and fitted into a theoretical balance of the acoustic radiation force and the drag force to obtain the acoustic energy density [32]. In the initial experimental trials, it was observed that

operating the device for long times tended to defocus the concentrated particle bands as the resonant frequency of the system changes. Hence, all the experimental results which are reported in this work were conducted with shorter run times (∼5–10 s) at lower applied voltages (10–15 V) to avoid this effect.

C. Sample preparation and operating parameters

To prepare bidisperse suspensions of known particle concentrations, particle powders containing monodisperse fluorescent polystyrene hard spheres ($\rho_p = 1050$ kg/m^3, CV: 10%) of sizes $2a_1 =$ 12 μm (red, Excitation/Emission: 542/612 nm) and $2a_2 = 6$ μm (green, Excitation/Emission: 468/508 nm) are added to a mixture of 15% iodixanol solution (OptiPrep) in deionized water and stirred until homogeneous. Here, the larger particle species are designated as "1" and the smaller particle species are designated as "2." The density gradient medium OptiPrep is added to increase the density [16] of the suspending fluid to $\rho_f = 1050$ kg/m^3 without a significant increase in the viscosity η, ensuring the particles become neutrally buoyant. The quantity of particle powders added is varied across different experiments to ensure the required particle concentrations are achieved. Two different values of the total volume fraction of the suspension ($\phi^0 = \phi_1^0 + \phi_2^0$) are used, $\phi^0 = 0.20$ and $\phi^0 = 0.30$, while the individual volume fractions of both the larger and smaller particle species are kept equal ($\phi_1^0 = \phi_2^0$). The experiments are conduced at a fixed suspension flow rate of $Q = 50$ μl/min. With average flow velocity computed as $u_{avg} = Q/(W \times H)$ and width of the channel as characteristic dimension, this corresponds to a hydrodynamic Reynolds number $\mathrm{Re} = \rho_f u_{avg} W/\eta_f \ll 1$. The streaming Reynolds number for Rayleigh streaming [33] can be computed using $\mathrm{Re}_\lambda = \rho_f u_{str} W/\eta_f$. Estimating the streaming velocity amplitude using $u_{str} = 4\psi E_{ac}/\rho_f c_f$, where ψ is a geometry dependent factor ($\psi = 3/8$ for a 1D standing wave [34]) and c_f is the speed of sound of the suspending fluid, we get $\mathrm{Re}_\lambda \ll 1$. Since we have $\mathrm{Re} \ll 1$ and $\mathrm{Re}_\lambda \ll 1$, inertial effects can be safely neglected. Furthermore, in 1D BAW resonance, the effect of Rayleigh streaming on the focusing of particles generally dominate over acoustic radiation force only when working with particles of small sizes (<2 μm). The critical particle diameter below which particle motion is dominated by acoustic streaming is theoretically given by [35] $a_{cr} = \sqrt{12\psi\nu/\pi\varphi f}$, where ν is the kinematic viscosity of the fluid, φ is the acoustic contrast factor, and f is the frequency of actuation. Substituting the values used in the present study, we get critical particle diameter $a_{cr} \approx 2.5$ μm. Here, the experiments involve particles of larger diameters (6 μm and 12 μm), and therefore we do not take the effects of acoustic streaming into consideration. The flow retention time within the channel length is also sufficiently low to preclude any settling of suspended particles.

III. THEORY AND NUMERICAL MODELING

Modeling of particle migration in bidisperse suspensions requires either of the two approaches: a multiscale approach where the particle equations are solved and coupled onto macroscale closures, or a continua-based approach [11,36]. Here, a continuum model is used because formulating at single particle level entails modeling the hydrodynamic effects, multiple acoustic scattering effects for each particle, in addition to the viscous and thermal dissipation for a very large number of particles, all of which makes modeling extremely challenging. At micron-sized scale, sheared high-concentration suspension flows can be adequately modeled by continua-based phenomenological diffusive flux models [11]. The dominant particle transport mechanisms for sheared flows in the presence of an imposed acoustic field are shear-induced migration and migration due to acoustic radiation forces. The formulation of the numerical model is discussed below.

A. Governing equations

The flow of the suspension is governed by the Navier-Stokes equations for fluid flow and the particle flux equations for the particle migration. These two sets of equations are interlinked

due to the dependence of local fluid properties on the particle concentrations. The continuity and momentum equations can be written as [37]

$$\frac{\partial \rho}{\partial t} + \nabla \cdot (\rho \boldsymbol{u}) = 0, \tag{1}$$

$$\frac{\partial (\rho \boldsymbol{u})}{\partial t} + \nabla \cdot (\rho \boldsymbol{u}\boldsymbol{u}) = -\nabla p + \nabla \cdot \eta[\nabla \boldsymbol{u} + (\nabla \boldsymbol{u})^T] + \boldsymbol{f}_r, \tag{2}$$

where η, ρ, and $\boldsymbol{u}$ are the suspension viscosity, density, and velocity, respectively, and p is the pressure. A suspended particle experiences a drag force when subjected to a migration force from an external field, and in turn, exerts a reaction force on the suspension [17]. The body force term in the momentum equation $\boldsymbol{f}_r = [\phi_i/(4/3\pi a_i^3)] \times F_{\text{rad,i}}$ quantifies this effect [17], where $F_{\text{rad,i}}$ is the acoustic radiation force acting on the particle, discussed later in Sec. III D. The equations governing the particle migration can be written in the form [38]

$$\frac{\partial \phi_i}{\partial t} + \boldsymbol{u} \cdot \nabla \phi_i = -\nabla \cdot \boldsymbol{J}_i, \tag{3}$$

where $\phi_i, \boldsymbol{J}_i$ are respectively the particle volume fraction and the net particle flux for particle species "i." The particle flux has contributions from the fluid-particle, particle-particle interactions, i.e., shear-induced migration, and also the acoustic radiation forces.

B. Shear-induced migration

In confined suspension flows involving micron-sized particles, hydrodynamic forces acting on the particles dominate over direct contact forces and colloidal forces [39]. A continua-based diffusive flux model (DFM) for these effects in a monodisperse suspension was developed by Phillips *et al.* [26] building on prior work by Leighton and Acrivos [25]. The particle migration is modeled in terms of two flux terms incorporating spatial gradients in the volume fraction (ϕ_i), shear rate ($\dot{\gamma}$), and suspension viscosity (η),

$$\boldsymbol{J} = \boldsymbol{J}_c + \boldsymbol{J}_\eta = -k_c a^2 \phi \nabla(\dot{\gamma}\phi) - k_\eta a^2 \dot{\gamma} \phi^2 \frac{1}{\eta} \nabla \eta, \tag{4}$$

where a is the particle radius, and k_c and k_η are phenomenological constants. Shauly *et al.* [27] expanded the formulation to model the flow of polydisperse suspensions of rigid spherical particles. The expression for particle flux is formulated as

$$\boldsymbol{J}_i = \boldsymbol{J}_{c,i} + \boldsymbol{J}_{\eta,i} = -k_c a_i \bar{a} \phi \nabla(\dot{\gamma}\phi_i) - k_\eta \bar{a}^2 \dot{\gamma} \phi \phi_i \frac{1}{\eta} \nabla \eta, \tag{5}$$

where $\bar{a}$ is the average particle size. For the present study involving bidisperse suspensions, $\bar{a}$ can be computed as $\bar{a} = \sum_{j=2} a_j \phi_j / \sum_j \phi_j$. The empirical values of $k_c = 0.41$ and $k_\eta = 0.62$ proposed in the original study [26] are retained. For the scale of particle sizes considered here ($a_i > 1\mu m$), Brownian effects will be negligible and are hence not considered. The definition of shear rate $\dot{\gamma}$ is modified to incorporate the anisotropy in diffusion. The diffusion in the plane of shear is assumed to be 1.5 times larger than that in the vorticity direction [40] and hence the shear rate is defined as

$$\dot{\gamma} = \frac{\left(\frac{\partial u_x}{\partial y}\right)^2 + 0.67\left(\frac{\partial u_x}{\partial z}\right)^2}{\sqrt{\left(\frac{\partial u_x}{\partial y}\right)^2 + \left(\frac{\partial u_x}{\partial z}\right)^2}}, \tag{6}$$

where u_x is the component of velocity in the flow direction. Since our numerical model is two-dimensional, $\partial u_x/\partial y$ is obtained from simulations, while $\partial u_x/\partial z$ is taken as $u_{\max}/(H/2)$, where H is the channel height.

C. Suspension viscosity

For the case of monodisperse suspensions, the viscosity of the fluid field varies with the local concentration of particles and can be modeled using a Krieger-Dougherty model [41],

$$\frac{\eta}{\eta_{\mathrm{f}}} = \left(1 - \frac{\phi}{\phi_{\max}}\right)^{-2.5\times\phi_{\max}}, \tag{7}$$

where η_{f} is the viscosity of particle-free suspending fluid and maximum packing fraction is taken as $\phi_{\max} = 0.64$. This simple relation works remarkably well even for general polydisperse suspensions where an appropriate value has to be used for the maximum packing fraction [42]. Specifically, for bidisperse suspensions, the maximum packing fraction is taken not as a constant value but dependent on the particle sizes and local particle concentrations. For a bidisperse suspension with ratio of the particle sizes $\sigma = a_2/a_1 < 1$, the maximum packing fraction is expressed by the heuristic relation [27]

$$\frac{\phi_{\max}}{\phi_{\max 0}} = 1 + \frac{3}{2}\left(\frac{\sigma - 1}{\sigma + 1}\right)^{3/2}\left(\frac{\phi_1}{\phi}\right)^{3/2}\left(\frac{\phi_2}{\phi}\right). \tag{8}$$

It can be seen that the maximum packing fraction for bidisperse suspensions is larger than that for a monodisperse suspension ($\phi_{\max 0}$) of equivalent volume fraction. This results in a relatively lower suspension viscosity for bidisperse suspensions at the same total volume fraction.

D. Acoustic radiation force

The primary acoustic radiation force on a particle in the dilute limit ($\phi \to 0$) under the effect of a one-dimensional acoustic standing-wave is given by [43]

$$F_{\mathrm{rad,i}} = 4\pi a_i^3 \varphi(\tilde{\kappa}, \tilde{\rho}) k E_{\mathrm{ac}} \sin(2ky). \tag{9}$$

Here, $k = \pi/\mathrm{W}$ is the wave number for a 1D standing half-wave along the width, $\varphi(\tilde{\kappa}, \tilde{\rho}) = \frac{1-\tilde{\kappa}}{3} + \frac{2(\tilde{\rho}-1)}{2\tilde{\rho}+1}$ refers to the acoustic contrast factor, which depends on the particle to suspending fluid density ratio ($\tilde{\rho} = \rho_{\mathrm{p}}/\rho_{\mathrm{f}}$) and compressibility ratio ($\tilde{\kappa} = \kappa_{\mathrm{p}}/\kappa_{\mathrm{f}}$). This expression works satisfactorily for modeling force on suspended particles which are near neutrally buoyant for which the effect of viscosity on the radiation force is negligible [44]. The viscous corrections will however become appreciable when the density of the particles are very different compared to that of the suspending fluid, for example, for the case of metallic particles. Equation (9) can be equivalently written in terms of the single particle acoustophoretic mobility from the relation ($F_{\mathrm{rad,i}} = 6\pi\eta_{\mathrm{f}} a_i u_{\mathrm{rad,i}}$, where η_{f} is the suspending fluid viscosity) as

$$u_{\mathrm{rad,i}} = \frac{2a_i^2 E_{\mathrm{ac}} \varphi k \sin(2ky)}{3\eta_{\mathrm{f}}}. \tag{10}$$

For the case of a homogeneous dense suspension, the secondary radiation force $F_{\mathrm{sec,i}}$ can be taken to be negligible in regions of uniform concentration profiles, $\nabla\phi_i \sim 0$, as forces from different particles in the vicinity negate each other by argument of symmetry. However, this is not the case for bidisperse suspensions due to the presence of different-sized particles and nonuniform concentration profiles. So here the secondary radiation force acting on the particle needs to be estimated. For simplicity, only the force acting in the direction of the acoustic wave, i.e., along y, is considered. For neutrally buoyant particles of different radii a_i and a_j, the force acting on the particle pair can be written as [45,46]

$$F_{\mathrm{sec,ij}} = -4\pi a_i^3 a_j^3 \frac{\omega^2 \rho_{\mathrm{f}} (\kappa_{\mathrm{p}} - \kappa_{\mathrm{f}})^2}{9d^2} p_1^2(y), \tag{11}$$

where d is the interparticle distance. The smallest value of interparticle distance $d = a_i + a_j$ is used in the model and the pressure field is taken as [47] $p_1 = p_{\mathrm{a}} \sin(ky)$ where p_{a} is the pressure

amplitude. Using the relations $\omega = kc_\mathrm{f}$, $\kappa_\mathrm{f} = 1/\rho_\mathrm{f} c_\mathrm{f}^2$, and acoustic energy density $E_\mathrm{ac} = p_\mathrm{a}^2/4\rho_\mathrm{f} c_\mathrm{f}^2$, and since components due to both force types *i*-*i* and *i*-*j* contribute to particle mobility, the secondary radiation force can be written in terms of an equivalent acoustophoretic mobility for particle species "*i*" as

$$u_{\mathrm{sec,i}} = \sum_j \frac{4a_i^2 a_j^3}{9d^4\eta_\mathrm{f}} E_\mathrm{ac} \left(\frac{\rho_\mathrm{p}}{\rho_\mathrm{f}} - 1\right)^2 \sin^2(ky). \tag{12}$$

E. Hindered particle mobility and particle fluxes

As compared to a dilute suspension, the mobility of a particle is significantly lower in a dense suspension due to the hydrodynamic interaction between different particles and the increase in viscosity in the suspension [48]. To model the reduced acoustophoretic particle mobility in a dense suspension, the dilute-limit particle mobility [Eqs. (10) and (12)] needs to be multiplied by an appropriate hindered mobility coefficient which accounts for this reduction. There are different expressions for this coefficient reported in literature, from studies on sedimentation of suspensions. The sedimentation rate of a particle in a dense suspension is lower due to other particles in its vicinity, and a hindered mobility coefficient quantifies this effect. For the case of polydisperse suspensions with n different particle species, coefficients of the form $f_{h,i} = 1 + \sum_{j=1}^{n} S_{ij}\phi_j$ were proposed [49,50] where S_{ij} are the sedimentation coefficients. This expression is accurate in systems where particle concentrations are relatively low ($\phi_i < 0.2$) but fails for more concentrated suspensions. In this study, a modified expression for hindered mobility coefficient [51] is used, which is applicable even at higher particle concentrations, as reported in previous studies [52],

$$f_{h,i} = (1-\phi)^{-S_{ii}} \left[1 + \sum_{j\neq i} (S_{ij} - S_{ii})\phi_j\right]. \tag{13}$$

The coefficients for the case of a bidisperse suspension can be taken as [51] $S_{11} = S_{22} = -5.6$ and $S_{ij} = -3.5 - 1.10\sigma - 1.02\sigma^2 - 0.002\sigma^3$ where $\sigma = a_j/a_i < 1$ is the particle size ratio. Setting $\sigma = 1$, the values of effective mobility obtained from the above expression are identical to that obtained numerically by Ladd [53] for monodisperse suspensions (see Supplemental Material Fig. S2 [31]).

The particle flux due to the primary radiation force can now be defined in terms of the single-particle acoustophoretic mobility by multiplying with the hindered mobility coefficient as a prefactor,

$$J_{\mathrm{rad,i}} = f_{\mathrm{h,i}} u_{\mathrm{rad,i}} \phi_i. \tag{14}$$

Likewise, the particle flux due to secondary radiation force can be written as

$$J_{\mathrm{sec,i}} = \sum_j f_{\mathrm{h,i}} u_{\mathrm{sec,i}} \phi_i \nabla\phi_j (a_i + a_j). \tag{15}$$

The dimensionless factor $\nabla\phi_j(a_i + a_j)$ scales for the presence of asymmetry in the vicinity and varies between 0 and 1. In regions with large asymmetry, this factor becomes highest and takes low values in regions where concentration gradients are also low.

As the flow develops, the gradients in particle volume fractions in lateral direction are much larger than gradients along the flow direction ($\partial\phi_i/\partial y \gg \partial\phi_i/\partial x$), and hence it suffices to consider the particle flux due to shear-induced migration only along y. Moreover, since we consider a one-dimensional standing acoustic wave, the contribution of acoustophoretic force to particle flux is also restricted to y. The total particle flux along y for particle species "*i*" can thus be expressed as a

summation of Eqs. (5), (10), and (12),

$$J_i = -k_c a_i \bar{a}\phi \frac{\partial}{\partial y}(\dot{\gamma}\phi_i) - k_\eta \bar{a}^2 \dot{\gamma}\phi\phi_i \frac{1}{\eta}\frac{\partial \eta}{\partial y} + f_{\mathrm{h,i}} u_{\mathrm{rad,i}} \phi_i + \sum_j f_{\mathrm{h,i}} u_{\mathrm{sec,i}} \phi_i \frac{\partial \phi_j}{\partial y}(a_i + a_j). \tag{16}$$

It is to be noted that this formulation reduces to that for monodisperse suspensions by setting $a_2 = a_1$.

F. Boundary and initial conditions

The equations are solved in a two-dimensional domain of dimensions 400 μm × 400 μm with flow along the x direction and the acoustic standing wave along the y direction [see Fig. 1(c)]. To model the flow along a long channel, periodic boundary conditions are applied in the flow direction, where a pressure difference (Δp) is specified through a trial-and-error approach to obtain an average flow velocity corresponding to the experimental flow rate. The governing equations are subject to the following initial and boundary conditions,

$$\boldsymbol{u} = 0 \qquad \text{at } y = -\mathrm{W}/2, \mathrm{W}/2, \tag{17}$$

$$\boldsymbol{J_i} = 0 \qquad \text{at } y = -\mathrm{W}/2, \mathrm{W}/2, \tag{18}$$

$$\phi_i = \phi_i^0 \qquad \text{at } t = 0, -\mathrm{W}/2 < y < \mathrm{W}/2, \tag{19}$$

$$\boldsymbol{u}_{\mathrm{x=0}} = \boldsymbol{u}_{\mathrm{x=L}}, \;\; p_{\mathrm{x=0}} + \Delta p = p_{\mathrm{x=L}}, \tag{20}$$

$$\phi_{\mathrm{i,x=0}} = \phi_{\mathrm{i,x=L}}, \;\; \boldsymbol{n} \cdot J_{\mathrm{i,x=0}} = -\boldsymbol{n} \cdot J_{\mathrm{i,x=L}}. \tag{21}$$

The profiles are quantified at different values of L_t/W, where $L_t(t)$ corresponds to the position of the fluid suspension after a retention time t and is computed using [38] $L_t(t) = \int_0^t u_{\mathrm{avg}}(t')dt'$. The term L_t/W is thus equivalent to the term x/W in experiments where x corresponds to the downstream distance from the channel inlet. Here, the numerical results are quantified for values up to $L_t/\mathrm{W} = 100$. For a 400 μm wide microchannel, this corresponds to a channel length of $L = 4$ cm, which is comparable to length used in general acoustofluidic devices. In the numerical formulation, the simulated concentration profiles may show sawtooth oscillations in regions where the particle volume fractions are very small ($\phi_i \to 0$). These oscillations are of purely numerical origin [17] and can be avoided by replacing the volume fraction (ϕ_i) in the formulation by an equivalent logarithmic variable, $\log(\phi_i/\phi_i^0)$, which ensures that the values of ϕ_i do not drop below zero.

The governing equations with the specified boundary and initial conditions are solved in weak form using the Mathematics: General Form Partial Differential Equation module of the finite-element based solver COMSOL Multiphysics [54]. The spatial domain is discretized into regular rectangular elements forming a structured mesh. Temporal discretization is performed using the backward implicit Euler method, and the timestep is adjusted by the solver to ensure specified tolerance and stability of the scheme. The equations are solved using the multifrontal massively parallel sparse (MUMPS) direct solver. To ensure grid independence of the numerical solution, the results obtained at different mesh sizes are compared with a highly refined reference mesh (see Supplemental Material Fig. S3 [31]).

IV. RESULTS AND DISCUSSION

A. Evolution of particle concentration profiles

For the flow of a suspension with individual particle volume fractions ($\phi_1^0 = \phi_2^0 = 0.15$) actuated at $E_{\mathrm{ac}} = 51$ J/m^3, the evolution of particle fluorescence intensity profiles (or concentration profiles) along the length of the channel at three different downstream locations from the inlet

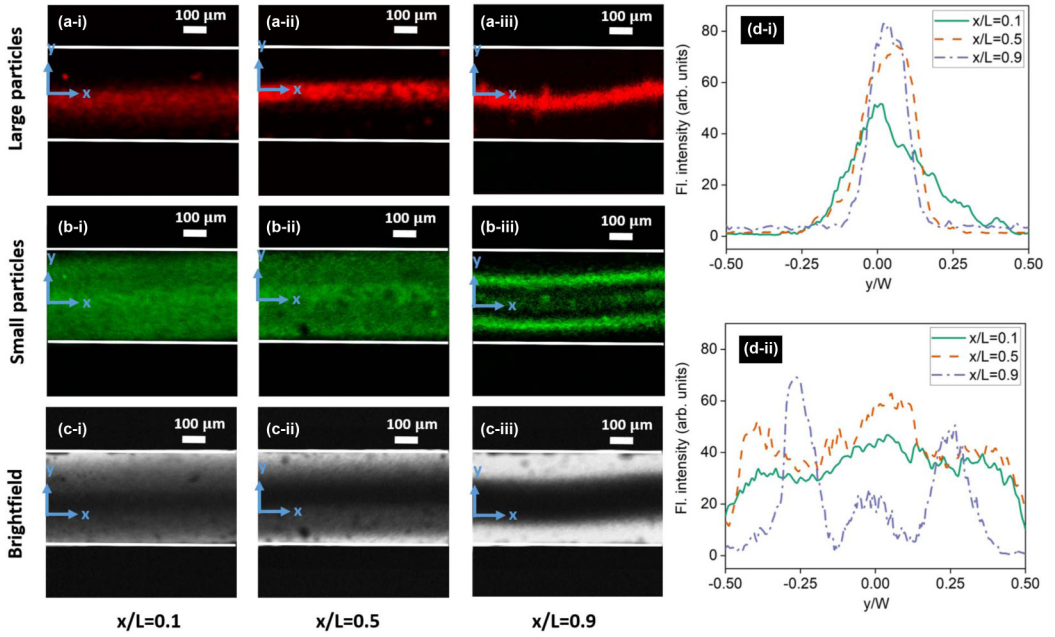

FIG. 2. For a total particle volume fraction $\phi^0 = 0.30$ with $\phi_1^0 = \phi_2^0 = 0.15$, fluorescent images are shown at three different downstream locations, $x/\mathrm{L} = 0.1, 0.5, 0.9$ for (a-i to a-iii) larger $2a_1 = 12$ µm particles (red fluorescent polystyrene microspheres), (b-i to b-iii) smaller $2a_2 = 6$ µm particles (green fluorescent polystyrene microspheres). (c-i to c-iii) Brightfield images indicate continued migration of both particles toward the channel center along the length. (d-i) Fluorescent intensity profiles for the larger particles taken along the width y, midway across each image indicates the larger particles get tightly packed into a narrow central band. (d-ii) Fluorescent intensity profiles for small particles show particle depletion at the channel center.

$(x/\mathrm{L} = 0.1, 0.5, 0.9)$ is presented in Fig. 2. The particle concentration distribution along the channel width y for both larger (red fluorescent) and smaller (green fluorescent) particles are computed by averaging over five different z slices spanning the depth of the channel ($z = 0$ to H). From a nearly uniform distribution along the width as the particles enter the channel [$\phi_1(y) = \phi_1^0$, $\phi_2(y) = \phi_2^0$ for $0 < y < \mathrm{W}$], particle migration toward the center commences under the combined action of shear-induced migration and acoustic radiation force. At a location close to the inlet, at $x/\mathrm{L} = 0.1$, the suspension begins to segregate and the larger red fluorescent particles start occupying the central region while the smaller particles remain mostly distributed across the width. Downstream at $x/\mathrm{L} = 0.5$, larger particles are seen to further concentrate towards the center and form a band of tightly packed particles. Computing the full-width at half maxima from the concentration profiles, it is seen that the width occupied by larger particles decreases only marginally further downstream (from 0.36W at $x/\mathrm{L} = 0.5$ to 0.34W at $x/\mathrm{L} = 0.9$) as the flow attains stable profiles.

The green fluorescent particles migrate relatively slower toward the center. The size scaling for particle flux ($J_i \sim a_i^2$) due to both shear-induced migration and acoustophoresis ensures faster migration of larger particles, which are disproportionately more enriched at the center of the channel, while the smaller particles are depleted in this region. This is because the high volume fraction of particles effectively prevent further migration of smaller green particles toward the center due to shear-induced migration. Close to the outlet at $x/\mathrm{L} = 0.9$, the smaller particles are seen to flank the central region of larger particles in two distinct bands as shown in Fig. 2. This is in contrast to the particle migration pattern observed under the influence of shear-induced migration alone (i.e., in the absence of acoustic field) where the larger particles migrate to the center with the smaller

particles being distributed almost uniformly across the width (see Supplemental Material Fig. S4 [31]). It is to be noted here that there is some amount of aggregation of smaller particles with larger particles at the channel center. This is because the particles which are present initially at the zero shear rate region at channel center mostly remain there and do not segregate. Additionally there could be some amount of agglomeration of both larger and smaller particles within the tubings before the suspension enters the main channel. It can also be seen that there is some focusing asymmetry resulting in wavy patterns, notably visible close to the outlet as seen in Fig. 2. The asymmetry stems from nonuniform pressure amplitudes along the length of the channel, deviation from resonant frequency due to shift in temperature [55], or differences in transducer position with respect to the channel which can form pinching regions as reported in previous studies [56,57].

B. Model validation

The numerical model is first validated with results from literature [28] for shear flow of binary mixture of particles. Later, the formulation of the acoustophoretic flux is verified with the current experimental results. The study by Semwogerere and Weeks [28] involves flow of a mixture of particles of sizes $a_1 = 1.5$ μm and $a_2 = 0.7$ μm, each with volume fraction $\phi_1^0 = \phi_2^0 = 0.1$. The small cross-sectional dimensions (50 μm × 500 μm) and large length (10 cm) leads to significant effect of shear-induced migration as the particles traverse the channel. The experimental concentration profiles at different downstream locations are compared with the predictions from the present model and shown in Fig. 3. The general trend in the evolution of particle concentration profiles shows a good agreement with the model. They differ only in a region very close to the walls. This deviation from experiments at the channel walls possibly arises from not considering effects on particles close to the walls from hydrodynamic particle-wall collisions/interactions, including adhesion and wall-normal lift forces. The numerical treatment usually involves incorporating small wall slip velocity or modifying the maximum packing fraction close to the walls [6,11]. These modifications are however not used in the present study since the acoustic forces drive the smaller particles away from the walls and toward the center unlike the case of shear-induced migration alone, where the smaller particles concentrate near the walls.

Introducing the acoustophoretic flux formulation, validation of the numerical model is performed by comparing the particle concentration profiles with experimental results. For suspension flow with spatially uniform volume fractions $\phi_1(y) = \phi_2(y) = 0.10$ at the inlet, actuated at $E_{\mathrm{ac}} = 51$ J/m^3, the stable concentration profiles are compared in Fig. 4. The particle fluorescent intensity data provides a measure of the local concentration/volume fraction of the particles. The intensity profiles from experiments are sampled near the outlet ($x/\mathrm{L} = 0.9$) along the dashed lines covering the width of the channel shown in Fig. 4. To smoothen the data, the intensity profile is averaged over a region which is 50 μm wide, centered along the dashed line. The experimental intensity profiles are then normalized with the corresponding maximum values to obtain the relative variation in fluorescent intensity along the width. It is then compared with the numerically obtained volume fractions, which are also normalized with the corresponding maximum values. The numerical profiles display no slope discontinuities, they exist as smooth profiles and show a similar pattern as the experimental profiles. The model captures the depletion of smaller particles at the center indicated by lower values of ϕ_2 similar to experiment, where there is a corresponding decrease in fluorescent intensity for smaller particles near the central region, at $y = 0$. This central region in Fig. 4 having a clear segregation of particles is narrower compared to Fig. 2, owing to a lower total volume fraction ($\phi^0 = 0.20$) which tends to focus the particles into a smaller width. The particle flux scales as $J_i \sim a_i^2$, hence as noted previously, the larger particles establish a stable concentration profile faster than smaller particles. In all the simulated cases, the larger particle volume fraction at the channel center is enriched. It is also worth noting that in stable profiles, neither the larger nor the smaller particles are present near the channel walls, and this justifies the exclusion of particle-wall interaction effects in the model. We compared the experimental profiles with the numerical predictions in Figs. 3 and 4 in terms of two-sample Chi-squared tests implemented in MATLAB. The hypothesis that there

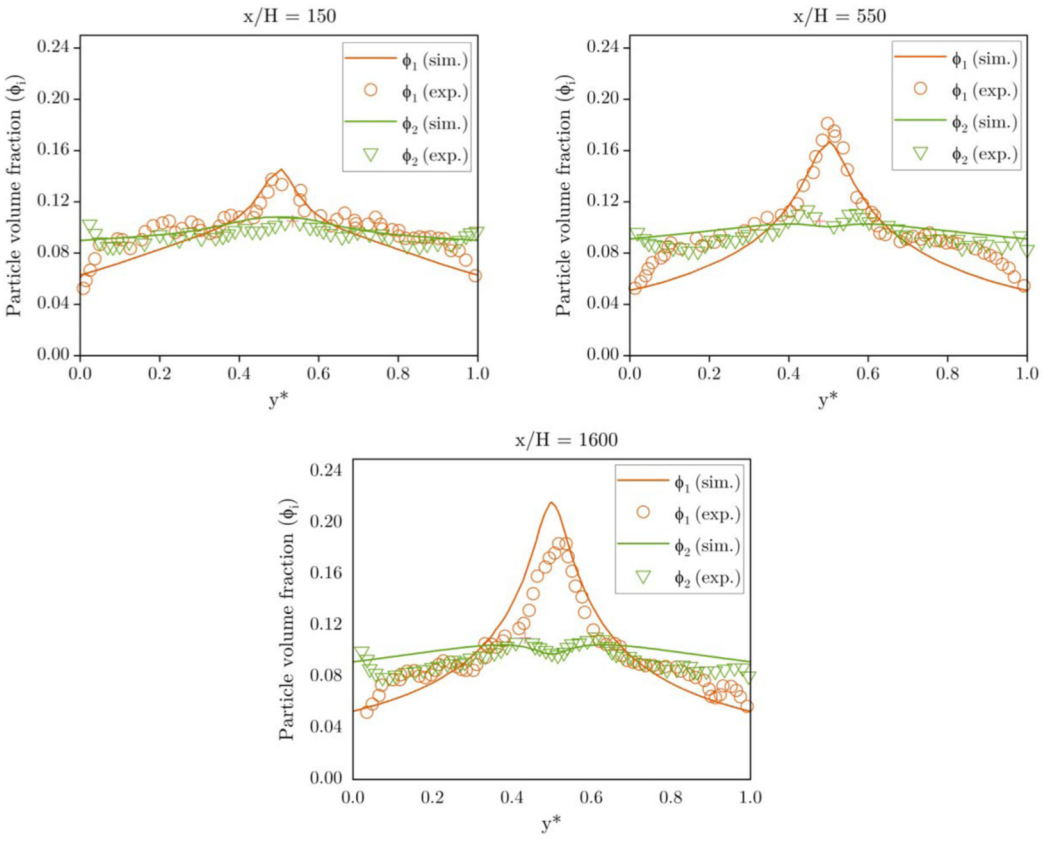

FIG. 3. Validation of the shear-induced migration formulation in the diffusive flux model with experimental results from previous study [28]. The local particle volume fractions (ϕ_1, ϕ_2) across the channel cross-section obtained from experiments are compared with numerical profiles at different downstream sections.

were no statistically significant differences between the experimental and numerical profiles is seen to be valid with significance level $\alpha = 0.05$.

Particle migration initiates in the main channel by the combined influence of acoustic field and the spatial variation in the shear rate and viscosity. Both the larger and smaller particle fluxes are highest initially as the suspension enters the main channel with spatially uniform volume fractions ϕ_1 and ϕ_2, and as the suspension approaches a stable profile, the net transverse flux on both larger and smaller particles gradually reduces to zero ($J_1 \to 0, J_2 \to 0$). At stable flow profile, the hindered acoustophoretic flux is balanced by the shear-induced migration flux. The different components of the particle flux for both the larger particles, J_1, and smaller particles, J_2, at stable condition are shown in Fig. 5. Here, only one half of the domain ($0 < y/\mathrm{W} < 0.5$) is shown due to inherent symmetry. The shear rate at the channel center in a Poiseuille flow is zero, and consequently the shear-induced migration components $J_{c,i}(y = 0)$ and $J_{\eta,i}(y = 0)$ are also zero. The component $J_{\eta,i}$ relates to the effect of gradients in the viscosity field on particle interactions, and results in a net particle drift in the direction of lower viscosity. As seen in Fig. 5, for both larger and smaller particles, $J_{\eta,i} > 0$, and tends to drive the particles away from the high viscosity central region toward the walls. The term $J_{c,i}$ relates to the frequency of particle interactions, and is higher in regions having large gradients in local particle concentration. Since the larger particles are enriched at the center, $J_{c,1} > 0$ tends to drive the particles away from the center. However, the small particles are depleted at the center, and consequently $J_{c,2} < 0$ tends to drive the particles from

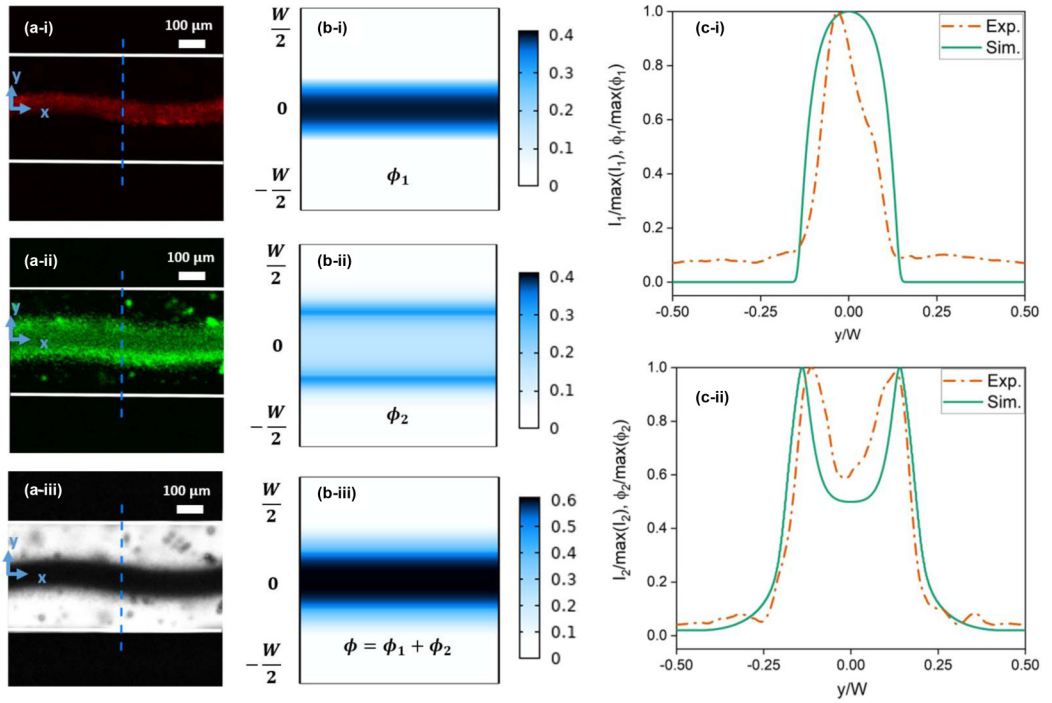

FIG. 4. For a total particle volume fraction $\phi^0 = 0.20$ with $\phi_1^0 = \phi_2^0 = 0.10$, the experimental (exp.) confocal fluorescent images of (a-i) larger $2a_1 = 12$ μm red fluorescent particles, (a-ii) smaller $2a_2 = 6$ μm green fluorescent particles, and (a-iii) brightfield image are shown. The contour plots of the simulated (sim.) particle volume fractions are shown for (b-i) larger particles, (b-ii) smaller particles, and (b-iii) combination of both. The normalized particle fluorescent intensity profile taken along the dashed lines in the experimental images are seen to compare well with normalized particle volume fractions from simulations for both (c-i) larger particles and (c-ii) for smaller particles.

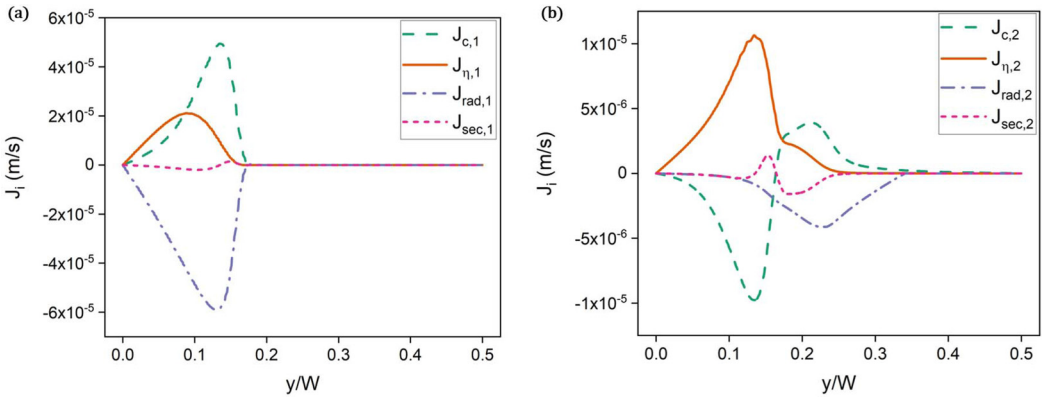

FIG. 5. The different components of the particle flux at stable condition for (a) larger particles (J_1) and (b) smaller particles (J_2) are shown. The balance of the different components leads to stable concentration profile. The flux components acting on the small particles ($J_2 \sim 10^{-6}$) are generally one order of magnitude smaller than that on the larger particles ($J_1 \sim 10^{-5}$).

the high concentration band flanking the center toward the central region. The acoustophoretic flux components $J_{\mathrm{rad,i}}$ and $J_{\mathrm{sec,i}}$ always force the particles toward the center and are influenced by the local values of mobility coefficients $f_{\mathrm{h,i}}$. $J_{\mathrm{rad,i}}$ and $J_{\mathrm{sec,i}}$ approach zero in regions of tight packing as $f_{\mathrm{h,i}} \to 0$. The stable volume fraction profile for the larger particles is achieved faster due to larger values of flux J_1, while the smaller particles take a longer time to reach stable profile, in line with experimental observations in Fig. 2.

C. Nondimensional parameters

To quantify the different results, nondimensional parameters are introduced which relate to the different operating parameters. In addition to the particle volume fractions (ϕ_1^0, ϕ_2^0), the particle size ratio ($\sigma = a_1/a_2$) also influences the relative rates of shear-induced migration. The effect of the imposed acoustic field can be quantified in terms of Strouhal number, which is defined as the ratio of the advection timescale (τ_{adv}) to the acoustophoretic migration timescale (τ_{mig}). The lengthscale of interest is half the channel width, W/2, which is the maximum lateral distance traversed by a particle, and the acoustophoretic migration timescale here is defined for the larger particle at dilute limit,

$$\tau_{\mathrm{adv}} = \frac{\mathrm{W}/2}{u_{\mathrm{avg}}}, \qquad \tau_{\mathrm{mig}} = \frac{\mathrm{W}/2}{2a_1^2\varphi E_{\mathrm{ac}}k/3\eta_{\mathrm{f}}}, \qquad \mathrm{St} = \frac{\tau_{\mathrm{adv}}}{\tau_{\mathrm{mig}}}. \tag{22}$$

Many acoustofluidic applications of interest involve enrichment of the suspended particle species within the channel and their extraction through the central outlet in a trifurcation. Hence, it is pertinent to quantify the enrichment of the particles within the central third of the channel width $-\mathrm{W}/6 < y < \mathrm{W}/6$.

The degree of focusing (ζ) and degree of segregation (χ) of the particles are defined as

$$\zeta_i = \frac{1}{\phi_i^0 \times \mathrm{W}} \int_{-\mathrm{W}/6}^{\mathrm{W}/6} \phi_i(y)dy, \qquad \chi = 1 - \frac{\zeta_2}{\zeta_1}. \tag{23}$$

$\zeta_1 = 1$, $\zeta_2 = 0$, and $\chi = 1$ indicate complete focusing of the larger particles and perfect segregation within the central third, i.e., the larger particles are wholly contained within the central region while the small particles are not present there. The evolution of the particle concentration can be quantified by these two nondimensional parameters ζ_1 and χ along the length of the channel.

D. Degree of particle focusing and segregation at different volume fractions

For a fixed particle radii ratio $\sigma^{-1} = 12\ \mu\mathrm{m}/6\ \mu\mathrm{m} = 2$ and $\mathrm{St} = 0.50$, i.e., parameters corresponding to experimental results in Fig. 4, the degree of focusing and segregation of particles along the length of the channel within the central third $-\mathrm{W}/6 < y < \mathrm{W}/6$ are quantified from the numerical model for different total volume fractions ($\phi^0 = 0.20, 0.30, 0.40$) as shown in Fig. 6. The individual particle volume fractions are kept the same ($\phi_1^0 = \phi_2^0 = \phi^0/2$). It is seen that with increasing values of L_t/W, the larger particles get more enriched at the center indicated by increased degree of focusing ζ_1. The rate of this enrichment decreases at higher L_t/W as particles already at the center approach maximum packing [$\phi(y = 0) \to \phi_{\mathrm{max}}$], and ζ_1 plateaus at different values of L_t/W depending on the composition of the suspension. For a total volume fraction of $\phi^0 = 0.20$, the suspension is fully focused ($\zeta_1 \approx 1$) at a downstream location corresponding to $L_t/\mathrm{W} \approx 50$. The value of L_t/W at which ζ_1 reaches a plateau is higher for a higher volume fraction. Lines a and b in Fig. 6 indicate reduced focusing of larger particles in a bidisperse suspension as compared to a monodisperse suspension of larger particles at the same individual volume fraction of 0.10. A similar trend is observed at higher volume fractions ($\phi_1^0 = \phi_2^0 = 0.15$) indicated by lines c and d where the difference in the degree of focusing between monodisperse and bidisperse suspensions is more pronounced due to a higher particle volume fraction. Comparing the degree of focusing at equal total volume fractions, lines e and f indicate that larger particles in bidisperse suspensions shows

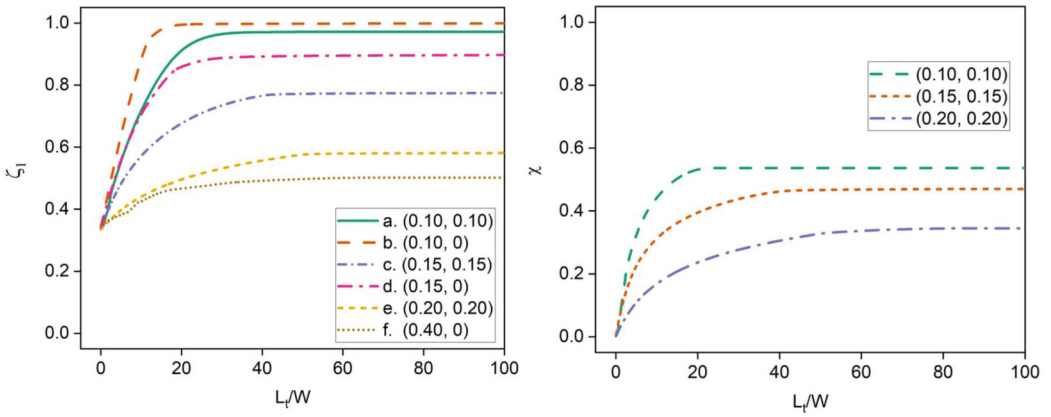

FIG. 6. The degree of focusing ζ_1 of larger particles is quantified for bidisperse suspensions (solid lines) with volume fractions (ϕ_1^0, ϕ_2^0) and monodisperse suspensions of large particles (dashed lines) at different particle volume fractions $(\phi_1^0, 0)$ at the same Strouhal number $\mathrm{St} = 0.50$. The degree of segregation χ at different volume fractions is also shown.

higher focusing as compared to a monodisperse suspension of large particles. This is expected as the large particle mobility is less hindered due to presence of smaller-sized particles in the suspension as compared to particles of the same size. The degree of segregation χ of the suspension is seen to increase initially with L_t/W, as the larger particles focus to the center pushing away the smaller particles toward the wall, before converging to stable values. Although smaller particles attain stable profile slower than larger particles, both ζ_1 and χ reach stable values at the same L_t/W, indicating that further changes in particle profile $\phi_2(y)$ occur outside of the central third. In general, the degree of segregation χ decreases with higher volume fractions, as smaller particles already at center have reduced mobility due to close packing.

E. Focusing and segregation at different acoustic energy density

Fixing the bulk suspension volume fraction ($\phi^0 = 0.30$) and the individual volume fractions of large ($2a_1 = 12$ μm) and small particles ($2a_2 = 6$ μm) to $\phi_1^0 = \phi_2^0 = 0.15$, the acoustic energy density is varied in the range $E_{\mathrm{ac}} = 0 - 76\ \mathrm{J/m^3}$. Equivalently, the Strouhal number changes from $\mathrm{St} = 0$ to $\mathrm{St} = 0.75$. It is observed from Fig. 7 that at higher values of St, both the degree of focusing ζ_1 and degree of segregation χ increase rapidly with L_t/W, due to increased acoustophoretic flux. At $\mathrm{St} = 0.20$, both ζ_1 and χ plateau close to $L_t/\mathrm{W} = 100$ indicating stable profiles. At higher values of St, stable profiles are attained at smaller L_t/W, while for lower St, ζ_1 and χ do not reach a plateau within the upper limit of L_t/W considered here. At high values of St, χ converges to a value of $\chi = 0.46$, which is the maximum degree of segregation achievable for the chosen particle sizes and volume fractions. It can be noted that at $\mathrm{St} = 0$, the particle flux from shear-induced migration alone drives focusing of larger particles to the center, and the enrichment and segregation at $L_t/\mathrm{W} = 100$ are close to $\zeta_1 \approx 0.4$ and $\chi \approx 0.18$, respectively.

F. Focusing and segregation at different particle size ratios

Keeping the larger particle size constant at $2a_1 = 12$ μm, the smaller particle size is varied so that the particle ratio $\sigma^{-1} = 1.5, 2.0, 3.0$, with constant total particle volume fraction $\phi^0 = 0.3$. As seen in Fig. 8, the degree of focusing ζ_1 and segregation χ at $\sigma^{-1} = 1.5$ and $\sigma^{-1} = 3.0$ show similar trends to that shown previously for $\sigma^{-1} = 2.0$. The degree of focusing for both $\sigma^{-1} = 1.5$ and $\sigma^{-1} = 3.0$ increases with length before plateauing close to $\zeta_1 = 0.80$ and $\zeta_1 = 0.60$ respectively. For higher difference in particle sizes, the degree of focusing is always higher, $\zeta_1(\sigma^{-1} = 3.0) >$

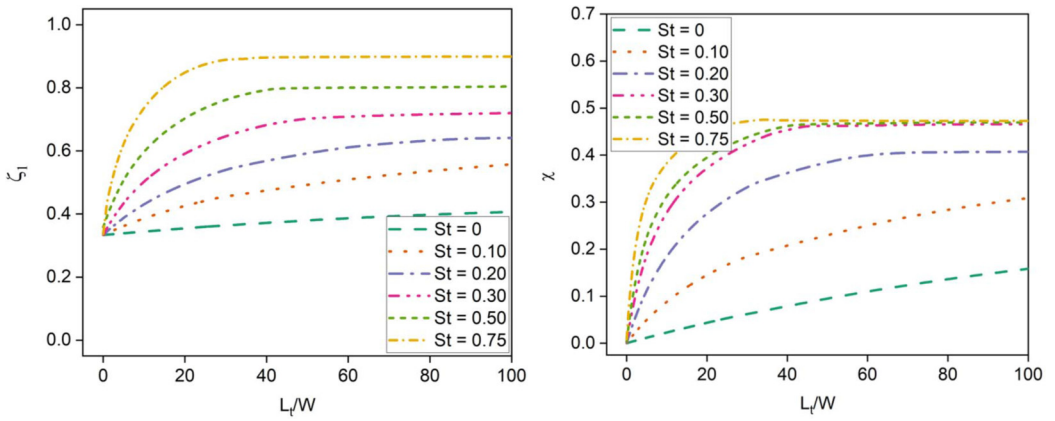

FIG. 7. Focusing and segregation behavior of the particles at different acoustic energy densities is quantified in terms of degree of focusing of larger particles (ζ_1) and degree of segregation (χ). In general, large values of St lead to both a higher degree of focusing and a higher degree of segregation.

$\zeta_1(\sigma^{-1} = 2.0) > \zeta_1(\sigma^{-1} = 1.5)$. This can be explained to arise from higher mobility of larger particles in Eq. (13) as the size of the smaller particle reduces. It also results in increased segregation with higher difference in particle sizes.

In general, the maximum degree of focusing and segregation of the suspension in the central third of the channel is seen to vary inversely with the total volume fraction, and directly with the Strouhal number and the particle size ratio. ζ_1 and χ increases with higher St and σ^{-1}, and reduces with increasing values of ϕ^0. Related, it is also seen that stable particle profiles are attained faster (at a smaller value of L_t/W) for increasing values of St and σ^{-1}. As the suspension becomes more concentrated, the particle volume fractions develop over a larger channel length before attaining stable profiles.

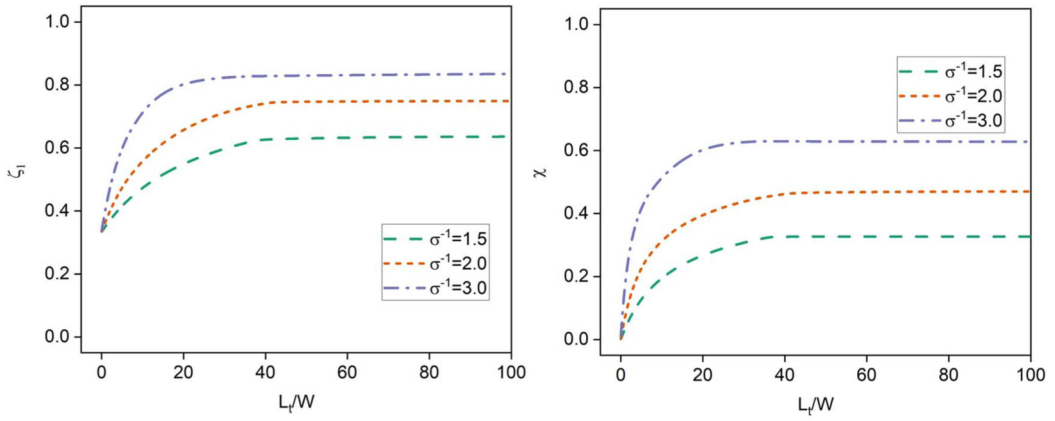

FIG. 8. The degree of focusing and segregation with L_t/W are shown for three different particle size ratios $\sigma^{-1} = a_1/a_2 = 1.5, 2.0, 3.0$. The larger particles focus to a narrower width as the size of the smaller particle reduces.

V. CONCLUSION

The focusing behavior of particles in bidisperse suspensions in a continuous flow inside a microchannel under the influence of a standing acoustic field is studied. The experiments reveal that the combined effect of acoustic radiation force and shear-induced migration influences particle motion and leads to stable particle concentration profiles. The larger particles form a highly concentrated band along the center of the channel with the smaller particles flanking this high concentration band on either side. A numerical formulation was developed based on diffusive flux model and the model predictions are compared to the experimental data, which showed a good match. Using the numerical formulation, the particle migration behavior at different bulk volume fractions, particle size ratios and acoustic energy densities were investigated and quantified in terms of nondimensional parameters, the degree of focusing of the particles, relating to enrichment, and their degree of segregation. The enrichment of larger particles and the segregation of the suspension is seen to increase with higher acoustic energy density and particle size ratios, and decrease with higher suspension volume fraction. The model underestimates the effect of acoustic interparticle interactions which possibly leads to the agglomeration of small particles at center as seen in Fig. 2. Nonetheless, the present model may prove useful in studies involving high concentration suspensions, for example, in designing for effective particle separation in microchannels, or in selective enrichment of suspended particle species. Although the model assumes hard spherical particles, it can be extended to biological cells by choosing appropriate fitting constants, particle concentration-viscosity relation, and relaxing the maximum packing fraction to higher values to account for deformability of bioparticles.

ACKNOWLEDGMENTS

A.K.S. thanks the Department of Science and Technology (DST), Govt. of India, for providing financial support in the inform of Swarnajayanti Fellowship via Grant No. DST/SJF/ETA-03/2017-18. The support from IIT Madras to the Micro Nano Bio-Fluidics Group under the funding for Institutions of Eminence Scheme of Ministry of Education, Govt. of India [Sanction No. 11/9/2019-0.3(A)] is also acknowledged.

[1] T. Laurell, F. Petersson, and A. Nilsson, Chip integrated strategies for acoustic separation and manipulation of cells and particles, Chem. Soc. Rev. **36**, 492 (2007).

[2] A. M. Van Dinther, C. G. Schroën, F. J. Vergeldt, R. G. Van Der Sman, and R. M. Boom, Suspension flow in microfluidic devices—A review of experimental techniques focussing on concentration and velocity gradients, Adv. Colloid Interface Sci. **173**, 23 (2012).

[3] T. Kulrattanarak, R. G. van der Sman, C. G. Schroën, and R. M. Boom, Classification and evaluation of microfluidic devices for continuous suspension fractionation, Adv. Colloid Interface Sci. **142**, 53 (2008).

[4] A. L. Graham, S. A. Altobelli, E. Fukushima, L. A. Mondy, and T. S. Stephens, Note: NMR imaging of shear-induced diffusion and structure in concentrated suspensions undergoing Couette flow, J. Rheol. **35**, 191 (1991).

[5] D. M. Husband, L. A. Mondy, E. Ganani, and A. L. Graham, Direct measurements of shear-induced particle migration in suspensions of bimodal spheres, Rheol. Acta **33**, 185 (1994).

[6] M. K. Lyon and L. G. Leal, An experimental study of the motion of concentrated suspensions in two-dimensional channel flow. Part 2. Bidisperse systems, J. Fluid Mech. **363**, 57 (1998).

[7] J. F. Brady, Macroscopic modeling of viscous suspension flows, Appl. Mech. Rev. **47**, S229 (1994).

[8] D. Leighton and A. Acrivos, The shear induced migration of particles in concentrated suspensions, J. Fluid Mech. **181**, 415 (1987).

[9] J. F. Morris, Toward a fluid mechanics of suspensions, Phys. Rev. Fluids **5**, 110519 (2020).

[10] D. Semwogerere, J. F. Morris, and E. R. Weeks, Development of particle migration in pressure-driven flow of a Brownian suspension, J. Fluid Mech. **581**, 437 (2007).
[11] H. M. Vollebregt, R. G. Van Der Sman, and R. M. Boom, Suspension flow modelling in particle migration and microfiltration, Soft Matter **6**, 6052 (2010).
[12] M. Antfolk and T. Laurell, Continuous flow microfluidic separation and processing of rare cells and bioparticles found in blood—A review, Analytica Chimica Acta **965**, 9 (2017).
[13] A. Nath, L. Malik, and A. K. Sen, Combined acoustic relocation and acoustophoretic migration for particle transfer between co-flowing fluids in a microchannel, Phys. Rev. Fluids **6**, 044201 (2021).
[14] B. Hammarström, T. Laurell, and J. Nilsson, Seed particle-enabled acoustic trapping of bacteria and nanoparticles in continuous flow systems, Lab Chip **12**, 4296 (2012).
[15] L. Malik, A. Nath, S. Nandy, T. Laurell, and A. K. Sen, Acoustic particle trapping driven by axial primary radiation force in shaped traps, Phys. Rev. E **105**, 035103 (2022).
[16] P. Augustsson, J. T. Karlsen, H. W. Su, H. Bruus, and J. Voldman, Iso-acoustic focusing of cells for size-insensitive acousto-mechanical phenotyping, Nat. Commun. **7**, 11556 (2016).
[17] M. W. Ley and H. Bruus, Continuum modeling of hydrodynamic particle-particle interactions in microfluidic high-concentration suspensions, Lab Chip **16**, 1178 (2016).
[18] S. Karthick and A. K. Sen, Role of shear induced diffusion in acoustophoretic focusing of dense suspensions, Appl. Phys. Lett. **109**, 014101 (2016).
[19] S. Karthick and A. K. Sen, Improved understanding of the acoustophoretic focusing of dense suspensions in a microchannel, Phys. Rev. E **96**, 052606 (2017).
[20] A. Nath and A. K. Sen, Acoustic Behavior of a Dense Suspension in an Inhomogeneous Flow in a Microchannel, Phys. Rev. Appl. **12**, 054009 (2019).
[21] H. Li, J. R. Friend, and L. Y. Yeo, Surface acoustic wave concentration of particle and bioparticle suspensions, Biomed. Microdevices **9**, 647 (2007).
[22] M. K. Tan, J. R. Friend, and L. Y. Yeo, Microparticle collection and concentration via a miniature surface acoustic wave device, Lab Chip **7**, 618 (2007).
[23] R. V. Raghavan, J. R. Friend, and L. Y. Yeo, Particle concentration via acoustically driven microcentrifugation: MicroPIV flow visualization and numerical modelling studies, Microfluid. Nanofluid. **8**, 73 (2010).
[24] Y. Akiyama, T. Egawa, K. Koyano, and H. Moriwaki, Acoustic focusing of microplastics in microchannels: A promising continuous collection approach, Sens. Actuators, B **304**, 127328 (2020).
[25] D. Leighton and A. Acrivos, Viscous resuspension, Chem. Eng. Sci. **41**, 1377 (1986).
[26] R. J. Phillips, R. C. Armstrong, R. A. Brown, A. L. Graham, and J. R. Abbott, A constitutive equation for concentrated suspensions that accounts for shear-induced particle migration, Phys. Fluids A **4**, 30 (1992).
[27] A. Shauly, A. Wachs, and A. Nir, Shear-induced particle migration in a polydisperse concentrated suspension, J. Rheol. **42**, 1329 (1998).
[28] D. Semwogerere and E. R. Weeks, Shear-induced particle migration in binary colloidal suspensions, Phys. Fluids **20**, 043306 (2008).
[29] M. Wiklund, H. Brismar, and B. Önfelt, Acoustofluidics 18: Microscopy for acoustofluidic micro-devices, Lab Chip **12**, 3221 (2012).
[30] W. G. Jerome and R. L. Price, *Basic Confocal Microscopy* (Springer, Berlin, 2018)
[31] See Supplemental Material at http://link.aps.org/supplemental/10.1103/PhysRevFluids.7.104201 for the fluorescent images of suspensions when they are flowed separately, comparison of expressions for hindered mobility coefficient, the grid convergence study, and experimental images showing particle migration in the absence of acoustic field.
[32] R. Barnkob, P. Augustsson, T. Laurell, and H. Bruus, Measuring the local pressure amplitude in microchannel acoustophoresis, Lab Chip **10**, 563 (2010).
[33] J. Friend and L. Y. Yeo, Microscale acoustofluidics: Microfluidics driven via acoustics and ultrasonics, Rev. Mod. Phys. **83**, 647 (2011).
[34] J. T. Karlsen, W. Qiu, P. Augustsson, and H. Bruus, Acoustic Streaming and its Suppression in Inhomogeneous Fluids, Phys. Rev. Lett. **120**, 054501 (2018).

[35] P. B. Muller, R. Barnkob, M. J. H. Jensen, and H. Bruus, A numerical study of microparticle acoustophoresis driven by acoustic radiation forces and streaming-induced drag forces, Lab Chip **12**, 4617 (2012).
[36] R. G. Van Der Sman and H. M. Vollebregt, Effective temperature for sheared suspensions: A route towards closures for migration in bidisperse suspension, Adv. Colloid Interface Sci. **185-186**, 1 (2012).
[37] M. Maxey, Simulation methods for particulate flows and concentrated suspensions, Annu. Rev. Fluid Mech. **49**, 171 (2017).
[38] B. Chun, J. S. Park, H. W. Jung, and Y.-Y. Won, Shear-induced particle migration and segregation in non-Brownian bidisperse suspensions under planar Poiseuille flow, J. Rheol. **63**, 437 (2019).
[39] R. G. Van Der Sman, Simulations of confined suspension flow at multiple length scales, Soft Matter **5**, 4376 (2009).
[40] X. Grandchamp, G. Coupier, A. Srivastav, C. Minetti, and T. Podgorski, Lift and Down-Gradient Shear-Induced Diffusion in Red Blood Cell Suspensions, Phys. Rev. Lett. **110**, 108101 (2013).
[41] I. M. Krieger and T. J. Dougherty, A mechanism for non-Newtonian flow in suspensions of rigid spheres, Trans. Soc. Rheol. **3**, 137 (1959).
[42] S. Pednekar, J. Chun, and J. F. Morris, Bidisperse and polydisperse suspension rheology at large solid fraction, J. Rheol. **62**, 513 (2018).
[43] H. Bruus, Acoustofluidics 7: The acoustic radiation force on small particles, Lab Chip **12**, 1014 (2012).
[44] M. Settnes and H. Bruus, Forces acting on a small particle in an acoustical field in a viscous fluid, Phys. Rev. E **85**, 016327 (2012).
[45] M. Groschl, Ultrasonic separation of suspended particles—Part I: Fundamentals, Acustica **84**, 432 (1998).
[46] S. Z. Hoque, A. Nath, and A. K. Sen, Dynamical motion of a pair of microparticles at the acoustic pressure nodal plane under the combined effect of axial primary radiation and interparticle forces, J. Acoust. Soc. Am. **150**, 307 (2021).
[47] H. Bruus, Acoustofluidics 2: Perturbation theory and ultrasound resonance modes, Lab Chip **12**, 20 (2012).
[48] R. Dorrell and A. J. Hogg, Sedimentation of bidisperse suspensions, Int. J. Multiphase Flow **36**, 481 (2010).
[49] G. K. Batchelor, Sedimentation in a dilute polydisperse system of interacting spheres. Part 1. General theory, J. Fluid Mech. **119**, 379 (1982).
[50] G. K. Batchelor and C. S. Wen, Sedimentation in a dilute polydisperse system of interacting spheres. Part 2. Numerical results, J. Fluid Mech. **124**, 495 (1982).
[51] R. H. Davis and H. Gecol, Hindered settling function with no empirical parameters for polydisperse suspensions, AIChE J. **40**, 570 (1994).
[52] M. Abbas, E. Climent, O. Simonin, and M. R. Maxey, Dynamics of bidisperse suspensions under Stokes flows: Linear shear flow and sedimentation, Phys. Fluids **18**, 121504 (2006).
[53] A. J. Ladd, Hydrodynamic transport coefficients of random dispersions of hard spheres, J. Chem. Phys. **93**, 3484 (1990).
[54] COMSOL Multiphysics 5.6, www.comsol.com (2020).
[55] J. Svennebring, O. Manneberg, and M. Wiklund, Temperature regulation during ultrasonic manipulation for long-term cell handling in a microfluidic chip, J. Micromech. Microeng. **17**, 2469 (2007).
[56] S. M. Hagsäter, A. Lenshof, P. Skafte-Pedersen, J. P. Kutter, T. Laurell, and H. Bruus, Acoustic resonances in straight micro channels: Beyond the 1D-approximation, Lab Chip **8**, 1178 (2008).
[57] O. Manneberg, B. Vanherberghen, B. Önfelt, and M. Wiklund, Flow-free transport of cells in microchannels by frequency-modulated ultrasound, Lab Chip **9**, 833 (2009).